COMMUNICATIONS IN SCIENCE AND TECHNOLOGY
Homepage: cst.kipmi.or.id

Erratum to: "Exploring fluidization dynamics and chemical performance in silicon tetrachloride (SiCl4) hydrochlorination processes within a fluidized bed reactor: Development and analysis of an Eulerian-granular model"

Erratum Information

Following the publication of this article (https://cst.kipmi.or.id/journal/article/view/1741), the authors identified that an incorrect set of simulation outputs and associated graphical results had been inadvertently included during manuscript submission. Consequently, several figures, numerical values, and discussions did not correspond to the final validated dataset generated using the adopted Eulerian–Granular computational model.

To address this issue, Table 3 was corrected to accurately identify the drag-force model employed in the simulations. Fig. 1–3 were revised to improve the presentation of the computational domain, grid-independence analysis, and model validation against experimental gas-temperature data. The validation results in Section 3.1 were updated, indicating deviations of approximately 2%, 4%, 6%, and 8% between simulation predictions and empirical calculations under the investigated operating conditions.

Fig. 4–6 were refined to provide more accurate representations of fluidization behavior, bubble formation, flow-regime transitions, bed-voidage evolution, and CFD-distributed behavior under different operating conditions. Corresponding discussions were updated for consistency without altering the overall scientific interpretation.

Fig. 7 and 8 were revised to improve the presentation of gas–solid heat-transfer coefficients and axial gas-temperature profiles, while Fig. 9 and 10 were updated to align the reaction-performance analysis with the validated simulation results. Minor revisions were also introduced throughout the manuscript, including figure captions, numerical values, graphical outputs, and related discussions, to ensure consistency with the validated dataset.

These corrections do not change the overall scientific conclusions of the study but improve the accuracy, consistency, and presentation of the reported results.

COMMUNICATIONS IN SCIENCE AND TECHNOLOGY
Homepage: cst.kipmi.or.id

Erratum to: "Exploring fluidization dynamics and chemical performance in silicon tetrachloride (SiCl4) hydrochlorination processes within a fluidized bed reactor: Development and analysis of an Eulerian-granular model"

Ekehwanh Rasheed[a], Saad Nahi Saleh[b], Jasim I. Humadi[c,*]

[a]*Chemical Engineering Department, Tikrit University, Tikrit 3400, Iraq*
[b]*Sustainable Energy Engineering Department, Tikrit University, Tikrit 3400, Iraq*
[c]*Department of Petroleum and Gas Refining Engineering, Tikrit University, Tikrit 3400, Iraq*

Article history:
Received: 31 May 2026 / Received in revised form: 19 June 2026 / Accepted: 20 June 2026

Abstract

The present work examines the complex fluidization pattern and reactive interactions of silicon tetrachloride ($SiCl_4$) during hydrochlorination in a fluidized-bed reactor (FBR), a system that remains difficult to model accurately. To address this gap, we develop a new Eulerian–granular CFD framework that for the first time couples the Eulerian–Eulerian fluid model with KTGF specifically for $SiCl_4$ hydrochlorination, enabling prediction capabilities that are unavailable in previous FBR studies. The validity of the model was confirmed through comparisons with empirical bed-expansion correlations and Hsu's gas-temperature data, that demonstrated strong agreement and the ability of the model to capture the coupled thermal–hydrodynamic behavior of the system. In addition to the conventional observations documented in previous studies, this study identifies distinct flow-regime transitions and bed-voidage evolution that are unique to $SiCl_4$. These findings demonstrated the impact of $SiCl_4$'s reactive transport behavior on fluidization stability. Under bubbling conditions, the model uncovered a characteristic $SiCl_4$ distribution pattern that more significantly enhanced gas–solid mixing in comparison to previous report. Additionally, it predicts rapid heat equilibration within ~13 mm of bed height - a behavior not documented in earlier hydrochlorination studies. Chemically, the model predicted a maximum $SiHCl_3$ concentration of 14.01% and an $SiCl_4$ conversion of 29.84%, thereby offering new mechanistic insight into how fluidization dynamics directly govern reaction performance. Overall, this work provides the first specialized CFD framework for $SiCl_4$ hydrochlorination, thus establishing a novel mechanistic understanding of its fluidization–reaction coupling. Furthermore, it offers a more accurate predictive basis for optimizing industrial FBR systems employed in silicon-based chemical manufacturing.

Keywords: Fluidization dynamics; silicon tetrachloride ($SiCl_4$); hydrochlorination process; Eulerian-granular model

1. Introduction

Polycrystalline silicon is a key raw fabric employed in the synthesis of monocrystalline silicon materials that are critical for the fabrication of both semi-conductor tool and solar cell [1,2]. The Siemens process [3] remains an imperative commercial approach to produce polysilicon, utilizing chemical vapor deposition (CVD) of purified trichlorosilane ($SiHCl_3$) and hydrogen (H_2) within a Siemens reactor. This method has been demonstrated to be effective and reliable, with a proven capacity to constantly produce excessive-purity polysilicon [4]. However, a major disadvantage of the Siemens method is the substantial amount of silicon tetrachloride ($SiCl_4$) required as a derivative [5]. Should $SiCl_4$ not properly processed, there will be a considerable loss of valuable silicon resources will be lost and extreme environmental and health risks will be posed by the substance in view of its exceptionally reactive and corrosive properties [6,7]. Consequently, the development of efficient strategies for the recycle and reuse of $SiCl_4$ has become a critical priority in polysilicon production.

Currently, hydrogenation, a process in which $SiCl_4$ is reacted with hydrogen to regenerate $SiHCl_3$, is seen as the most efficient approach to managing $SiCl_4$. This method is highly advantageous for providing a sustainable source of $SiHCl_3$ feedstock while simultaneously mitigating the environmental hazards associated with $SiCl_4$ accumulation. The fluidized bed reactor (FBR) serves as the core technology for $SiCl_4$ hydrogenation, offering superior gas-solid contact efficiency and enhanced mass transfer characteristics [8]. The initial reaction governing this transformation is illustrated in Eq. (1). A subtle version of the hydrogenation technique is hydrochlorination [9], which entails the creation of hydrogen

* Corresponding author.
Email: jasim_alhashimi_ppe@tu.edu.iq
https://doi.org/10.21924/cst.11.1.2026.2008

chloride (HCl) as an additional reactant [10]. The center reaction governing the hydrochlorination manner is presented in Eq. (2).

$$3SiCl_4+2H_2+Si \rightarrow 4SiHCl_3 \quad (1)$$

$$2SiCl_4+H_2+Si+HCl \rightarrow 3SiHCl_3 \quad (2)$$

For further optimization of this process, a thorough analysis of several critical factors is deemed pivotal. Firstly, it is vital to ensure the structural stability of the FBR to withstand prolonged operational conditions without compromising performance. Secondly, it is important to ensure uniform flow distribution within the reactor to prevent localized overheating and enhance reaction uniformity. Thirdly, the heat transfer efficiency of the system must be optimized to facilitate rapid thermal equilibrium and improve energy utilization. Ultimately, a thorough evaluation of the chemical performance is required to maximize $SiCl_4$ conversion rates and enhance product yield. Addressing these key parameters will facilitate the development of a more efficient and sustainable hydrochlorination process, which will, in turn, contribute to both the advancement of the industrial utilization of $SiCl_4$ and the development of high-purity polysilicon production. Lee et al. [11] examined the hydrogenation of $SiCl_4$ using a carbon-based totally catalyst, demonstrating that minimizing the reverse response among $SiHCl_3$ and HCl extensively improves $SiHCl_3$ yield. Similarly, Jain et al. [12] explored silicon hydrochlorination, determining reaction rate constants for the interaction between Si and HCl on a silicon substrate, even as Becker et al. [13] developed a comprehensive kinetic modeling to simulate the hydrochlorination of $SiCl_4$ and explored the impact of different operational parameters on $SiHCl_3$ yield. Despite the significant contribution of these studies to the understanding of reaction kinetics and thermodynamic constraints, they frequently neglect the role of transfer phenomena, such as fluid flow dynamics, heat transfer, and mass transport within the reactor. Given that chemical reactions in an FBR occur in a multiphase environment where gas-solid interactions are highly dynamic, neglecting these factors can lead to incomplete process optimization. Consequently, research must move beyond purely thermodynamic and kinetic analyses to incorporate a more detailed understanding of fluidization behavior and its direct impact on reaction efficiency.

In recent years, there has been a increasing interest in both experimental and theoretical research aimed at investigating knowledge fuel-solid fluidization conducts in fluidized mattress reactors (FBRs) [14-16]. Of these studies, Chein et al. [17] utilized numerical simulations to examine combustion structures in conventional bubbling fluidized beds (BFBs) and effervescent fluidized beds with inner particle stream (ICBFBs). The consequences of this process highlight the significant enhancement in reactant mixing that is achieved by the ICBFB design, thereby enhancing chemical reaction efficiency. The research by Pottimurthy et al. [18] provided further insight into gas-strong interplay mechanisms. They performed precise three-dimensional imaging analyses to research the distribution of strong volume fraction in slugging fluidized beds. Their work delineated three notable fluidization zones: bottom fluidization, fuel slug, and solid slug. The study revealed the impact of slugging velocity on the duration of the gas slug period. This finding is critical for the optimization of gas-segment response zones. Furthermore, Liu et al. [19] employed an Eulerian–Eulerian two-fluid framework integrated with population balance equations to model the growth behavior of silicon particles during chemical vapor deposition in slugging FBRs. Their simulations incorporated factors such as surface deposition and particle aggregation, with results validated against experimental flow and heat transfer data.

A huge range of research has investigated vital fluidization parameters along with fluidization speed [21,22], mattress enlargement height [23,24], solid quantity fraction, and voidage [25,26]. These efforts have led to substantial enhancement in our understanding of flow conduct and thermal dynamics within fluidized bed reactors (FBRs). However, research particularly focused on the fluidization conduct of $SiCl_4$ hydrochlorination procedures, so far, remained limited [27,28]. Liu et al. [29] utilized computational fluid dynamics (CFD) to analyze the impact of baffle designs on $SiCl_4$ hydrogenation in an FBR. Their findings revealed that the incorporation of louvered baffles led to a substantial enhancement in reaction performance, resulting in enhanced $SiCl_4$ conversion rates in comparison to channel baffles. Despite the critical insights provided by these studies into FBR flow regimes, heat switch mechanisms, and manner stability, the precise connection among fluidization conduct and chemical reaction efficiency in $SiCl_4$ hydrochlorination remains to be fully elucidated. The objectives of this study is to address this critical gap by using developing a sophisticated Eulerian–Granular Model (EGM) and using CFD simulations to discover the effects of fluidization speed.

2. Model Description

2.1. CFD model

2.1.1. Eulerian-granular model

The Eulerian-Granular Model (EGM) is a sophisticated approach to simulating multiphase flow dynamics within fluidized bed reactors (FBRs). This model is developed by combining the Eulerian–Eulerian two-fluid model (TFM) with the kinetic theory of granular flow (KTGF), thereby enabling a more accurate representation of gas-solid interactions within the reactor environment. The EGM framework is particularly well-suited for capturing the complex behavior of dispersed solid particles within a continuous gas phase, rendering it an indispensable tool for analyzing fluidization dynamics, mixing efficiency, heat transfer, and reaction kinetics in $SiCl_4$ hydrochlorination processes. The Eulerian–Eulerian approach is predicated on the premise that both the gas and solid phases are treated as continuous interpenetrating media, where each phase is described using its own set of conservation equations, thus allowing for a detailed examination of the phase interactions without a need for explicit tracking of individual particles, which will otherwise be computationally prohibitive for large-scale industrial reactors. The granular phase behavior in this model is governed by the kinetic theory of granular flow (KTGF), which extends classical kinetic gas theory to describe the motion and energy dissipation of colliding solid particles.

In contrast to more simplistic empirical drag models, KTGF considers a more comprehensive set of parameters, including particle velocity distributions, collision frequencies, restitution coefficients, and solid stress tensors. This enhanced framework enables a more physically realistic depiction of solid-phase momentum transfer and energy dissipation.

The continuity equations are of fundamental role in capturing mass conservation for both gas and solid phases within the FBR. These equations describe how the volume fractions and densities of the gas and solid components evolve over time and space, accounting for mass exchange processes between the two phases. The terms ms and mg represent the interphase mass transfer rates, characterizing how mass is exchanged between the gas phase (denoted by the subscript g) and the solid phase (denoted by the subscript s) due to chemical reactions, phase changes, or adsorption/desorption phenomena. Additionally, α represents the volume fraction of each phase, while ρ denotes the respective phase densities. These parameters are essential for defining the spatial distribution of the reactants and products within the reactor, influencing the overall reaction efficiency and conversion rates.

The Eulerian-Granular Model (EGM) provides an advanced numerical framework for simulating the fluidization behavior, reaction kinetics, and thermal dynamics of the $SiCl_4$ hydrochlorination process in fluidized bed reactors. By leveraging this model, researchers can gain valuable insights into optimal reactor operating conditions, fluidization stability, and interphase mass transfer phenomena, thereby paving the way for more efficient and scalable polysilicon production technologies.

$$\frac{\partial}{\partial t}\left(a_g p_g\right) + \nabla.\left(a_g p_g{}^{\vec{v_g}}\right) = m_{gs} \tag{3}$$

$$\frac{\partial}{\partial t}\left(a_s p_s\right) + \nabla.\left(a_s p_s{}^{\vec{v_s}}\right) = m_{sg} \tag{4}$$

where a_g is the gas phase volume fraction, a_s is the solid phase volume fraction, ρg and ρs are the densities of the gas and solid phases, respectively, $\vec{v}g$ and $\vec{v}s$ are the velocities of the gas and solid phases, ∂/∂t represents the time derivative, ∇· denotes the divergence operator, mgs is the mass transfer rate from the gas phase to the solid phase, and msg is the mass transfer rate from the solid phase to the gas phase .

The momentum equations, given in Eq. (5-8), describe the forces performing on both the gasoline and solid stages.

$$\frac{\partial}{\partial t}\left(a_g p_g \vec{v_g}\right) + \nabla.\left(a_g p_g v_g \vec{v_g}\right) = -a_g p_g g + \nabla t_g - a_g \nabla \mathrm{p} + K_{gs}\left(\vec{v_s} - \vec{v_g}\right) - m_{gs}\vec{v_g} \tag{5}$$

$$t_g = a_g \mu_g\left(\nabla_{\vec{v_g}} + \nabla_{\vec{v_g}}^{\mathrm{T}}\right) \tag{6}$$

$$\frac{\partial}{\partial t}\left(a_s p_s \vec{v_s}\right) + \nabla.\left(a_s p_s \vec{v_s}\,\vec{v_s}\right) = -a_s p_s + \nabla t_s - a_s \nabla \mathrm{p} + K_{sg}\left(\vec{v_s} - \vec{v_g}\right) - m_{sg}\vec{v_s} \tag{7}$$

$$\tau \mathrm{s} = a_s \mu_s\left(\nabla_{\vec{v_s}} + \nabla_{\vec{v_s}}^{T}\right) + a_s\left(\lambda_s - \frac{2}{3}\mu_s\right)\nabla_{\vec{vs}} I \tag{8}$$

where $\vec{v}g$ and $\vec{v}s$ are the velocity vectors of the gas and solid phases, τg and τs are the stress tensors of the gas and solid phases, μg and μs are the dynamic viscosities of the gas and solid phases, λs is the bulk viscosity of the solid phase, I is the identity matrix, g is the gravitational acceleration vector, ∇p is the gradient of pressure in the reactor, Kgs are the interphase momentum transfer coefficients (drag coefficients) between the gas and solid phases, tg and ts are the viscous stress tensors for the gas and solid, and the terms $mgs\vec{v}g$ and $msg\vec{v}s$ account for the momentum exchange associated with mass transfer between the phases.

The energy equations are presented in Eq. (9-11) where the subscript "m" represents both the gas and solid phases. These equations govern enthalpy, heat capacity, turbulent kinetic energy, and temperature distribution within the system.

$$\frac{\partial}{\partial t}(\alpha_m \rho_m h_m) + \nabla.(a_m p_m \overrightarrow{v_m} h_m) = a_m \frac{\partial p_m}{\partial t} + t_m \nabla.\overrightarrow{v_m} - \nabla \cdot \mathrm{qm} - (\mathrm{Q}_{gs} + m_{gs}\mathrm{h}_{gs} - m_{sg}\mathrm{h}_{sg}) \tag{9}$$

$$h_m = \int_{T_{ref}}^{T} C_{p,m}{}^{dT} \tag{10}$$

$$\mathrm{q}_m = -\alpha_m K_m \nabla T_m \tag{11}$$

where αm is the volume fraction of phase m (which can be gas or solid), ρm is the density of phase m, hm is the specific enthalpy of phase m, Cp,m being the specific heat capacity at constant pressure of phase m, and Tref is the reference temperature. $\vec{v}m$ is the velocity vector of phase m, tm is the viscous stress tensor of phase m, qm is the heat flux vector due to conduction within phase m, Qgs is the interphase heat transfer rate between gas and solid phases, and hgs and hsg represent the enthalpies associated with mass transfer from the gas to the solid phase and from the solid to the gas phase, respectively.

The solid pressure and radial distribution functions are mathematically defined in Eq. (12) and (13). In these expressions, (Θ_s) denotes the granular temperature, which characterizes the average kinetic energy of the solid particles within the system and term ($e_{\{ss\}}$) represents the particle-particle restitution coefficient, a crucial parameter that quantifies the degree of inelasticity in collisions between particles, influencing energy dissipation and overall system dynamics. Furthermore, (g_0) is the radial distribution function, which describes the spatial arrangement and local packing density of particles, playing a significant role in determining inter-particle interactions and pressure variations in granular flows.

$$p_s = \alpha_s p_s \Theta_s + 2p_s(1 + e_{ss}) a_s^2 g 0_{,ss} \Theta_s \tag{12}$$

$$\mathrm{g}\,0 = \left[1 - \left(\frac{\alpha \mathrm{s}}{as,max}\right)^{1/3}\right]^{-1} \tag{13}$$

The solid shear stress, which is comprised of collisional viscosity, kinetic viscosity, and frictional viscosity, is expressed in Eq. (14–17). In these equations, ds represents the diameter of the strong debris.

$$\mu_s = \mu_{s,col} + \mu_{s,Kin} + \mu_{s,fr} \tag{14}$$

$$\mu s, \mathrm{col} = \frac{4}{5} a_s p_s d_s \, g_{0,ss}(1 + e_{ss}) \sqrt{\frac{\Theta s}{\pi}} \quad (15)$$

$$\mu s, \mathrm{kin} = \frac{10 p_s d_{s\sqrt{\Theta s \pi}}}{96 a_s (1+e_{ss}) g_{0,ss}} \left[1 + \frac{4}{5} g_{0,ss} a_{s(1+e_{ss})}\right]^2 \quad (16)$$

$$\mu s, \mathrm{fr} = \frac{p_s sin\varphi}{\sqrt[2]{I_{2D}}} \quad (17)$$

where μ_s is the total dynamic viscosity of the solid phase, which is comprised of three contributions: $\mu_{s,col}$ is the collisional viscosity, $\mu_{s,kin}$ is the kinetic viscosity, and $\mu_{s,fr}$ is the frictional viscosity. In the collisional viscosity term, ds is the diameter of the solid particles, $g_{0,ss}$ is the radial distribution function at contact for solids, ess is the restitution coefficient of particle collisions, and Θs is the granular temperature of the solid phase. In the kinetic viscosity term, as is the solid volume fraction, and the expression accounts for the effect of particle interactions on momentum transport due to random motion. The frictional viscosity $\mu_{s,fr}$ depends on the solid phase pressure p_s the internal friction angle ϕ, and the inertial number I_{2D}, capturing the contribution of enduring contacts and frictional effects in dense granular flows.

The concept of granular temperature, which quantifies the intensity of random particle motion in a fluidized system, is mathematically represented in Eq. (18). This parameter is a crucial factor in determining the kinetic energy distribution of solid particles, as it directly influences momentum transfer, phase interactions, and overall system stability. One of the primary sources of energy dissipation in granular flows is collisional dissipation, as illustrated by Eq. (19). This phenomenon, denoted as ⟦γΘ⟧ _s, is responsible for the energy lost due to inelastic particle collisions, which is a fundamental process governing particle clustering, agglomeration, and phase stability within the fluidized bed reactor (FBR). In addition to collisional dissipation, granular flow systems exhibit interphase energy transfer due to interactions between the gas and solid phases. This transfer, mathematically expressed in Eq. (20), is governed by the term φ_gs, which represents the exchange energy between the gas and solid phases. This parameter accounts for the momentum and thermal energy exchange that occurs as gas molecules interact with suspended solid particles in the fluidized bed. The efficiency of this gas-solid energy transfer is influenced by various factors, including particle size distribution, voidage, superficial gas velocity, and system pressure.

$$0 = (-p_s I + t_s)\nabla . v_s - \gamma\Theta_s + \varphi_{\mathrm{gs}} \quad (18)$$

$$\mathrm{r}\Theta_m = \frac{12(1-e^2{}_{ss} g_{0,ss})}{d_s \pi} a^2{}_{sPs} \Theta_s^{3/2} \quad (19)$$

$$\varphi_{\mathrm{gs}} = -3K_{gs}\Theta_s \quad (20)$$

where Θ_s is the granular temperature of the solid phase, representing the kinetic energy of particle velocity fluctuations. γ is defined as the collisional dissipation rate of granular energy resulting from inelastic particle collisions. Φgs is the energy exchange term between the gas and solid phases associated with granular motion. In Eq. (19), $r\Theta_m$ represents the generation rate of granular energy in phase mmm, a_{sPs} is the particle volume fraction in phase m, and the factor $(1-ess^2)g_{0,ss}$ captures energy loss due to inelastic collisions between particles. In Eq. (20), Kgs is the interphase momentum transfer coefficient (drag coefficient), whereas the term −3KgsΘs represents the dissipation of granular energy due to drag interaction with the gas phase.

2.1.2. Turbulence model

To accurately model turbulence behavior, this study adopted the Renormalization Group (RNG) k-ε turbulence model combined with a standard wall function to determine turbulent viscosity. This approach is well-suited for capturing complex flow characteristics in fluidized bed systems.

The governing transport equations for turbulence are expressed as follows:

$$\frac{\partial}{\partial t}(p_{m^k}) + \frac{\partial}{\partial x_i}(p_m K\overrightarrow{v_m}) = \frac{\partial}{\partial x_j}\left[\alpha_K \mu_{eff} \frac{\partial K}{\partial x_j}\right] + G_{k,m} - pm^{\varepsilon} \quad (21)$$

$$\frac{\partial}{\partial t}(pm^{\varepsilon}) + \frac{\partial}{\partial x_i}\left(pm^{\varepsilon \vec{v}}{}_m\right) = \frac{\partial}{\partial x_j}\left[\alpha_\varepsilon \mu_{\mathrm{eff}} \frac{\partial \varepsilon}{\partial \mathrm{x_j}}\right] + C_{1\varepsilon}\frac{\varepsilon}{\mathrm{k}} G_{\mathrm{k},m} - C_{2\varepsilon} pm \frac{\varepsilon^2}{\mathrm{k}} \quad (22)$$

where

- k refers the turbulent kinetic energy,
- ε refers the turbulent dissipation rate,
- $G_{k,m}$ is the production term of turbulent kinetic energy,
- M_{eff} is the effective dynamic viscosity.

The following expressions further describe the turbulence model:

$$d\left[p\frac{\mathrm{k}^2}{\sqrt{\varepsilon\mu}}\right] = 1.72v\sqrt{v^3 - 1 + C_v dv} \quad (23)$$

$$\mathrm{Cv}{\approx}100\ v = \frac{\mu_{\mathrm{eff}}}{\mu} \quad (24)$$

$$\mu\mathrm{t} = pC_\mu \frac{\mathrm{k}^2}{\varepsilon}, 0.0845 \quad (25)$$

where k is the turbulent kinetic energy, ε is the turbulent dissipation rate, and μ is the molecular (laminar) viscosity of the fluid. The ratio μ_{eff}, denoted as v, is the viscosity ratio, which incorporates both molecular and turbulent contributions. Cv is the viscosity correction factor, typically approximated as Cv≈100C, utilized to account for conditions of high viscosity. The term μt is defined as the turbulent eddy viscosity, which is measured using the turbulent kinetic energy and dissipation rate through the coefficient Cμ=0.0845. These relations constitute a component of the turbulence model utilized to describe momentum transport and turbulent mixing in multiphase flows. The constants employed in the model are as follows: C1ε=1.44 and C2ε=1.92

The RNG k-ε model provides an enhanced prediction of turbulence effects, particularly in highly rotational and shear-dominated flows. By incorporating modifications to the standard k-ε formulation, this model effectively accounts for rapid strain and vortex stretching, rendering it highly suitable for simulating the intricate flow dynamics present in fluidized bed reactors.

2.1.3. Drag model

The interphase exchange coefficient (Kgs) in this study was determined based on the empirical drag correlation proposed by Gidaspow et al. [35]. This model accounts for momentum exchange between the gas and solid phases and adapts to different flow conditions. The governing equations are presented as follows:

For cases where the gas volume fraction (αg) exceeds 0.8, the drag force is expressed as follows:

$$\mathrm{K_{gs}} = \frac{3}{4} C_D a_s a_g p_g \frac{|\vec{v_g} - \vec{v_s}|}{d_s} a_g^{-2.65}, a_g > 0.8 \qquad (26)$$

where:

- CD is the drag coefficient for spherical particles,
- $\mathrm{Re_s}$ is the Reynolds number of solid particles,
- αg and αs are the gas and solid volume fractions, respectively,
- ds represents the solid particle diameter, and
- ρg denotes the gas phase density.

The drag coefficient CDC follows the empirical correlation:

$$C_{D=\frac{24}{a_g R_e^s}[1+0.15(a_g R_e^s)^{0.687}]} \qquad (27)$$

For denser conditions where the gas volume fraction (αg) is 0.8 or lower, the drag coefficient is instead described by:

$$K_{gs} = 150 \frac{a_s(1-a_g)\mu g}{a_g a_s^2} + 1.75 \frac{a_s p_g |\vec{v}\, g - \vec{v}\, s|}{d_s}, a_{g \le 0.8} \qquad (28)$$

This Gidaspow drag model effectively bridges two widely used formulations:

- The Ergun equation, which dominates in highly packed systems, and
- The Wen & Yu correlation, which better describes dilute gas–solid flows.

The integration of these two approaches within this model provides an accurate representation of momentum transfer, thereby capturing the effects of particle clustering and fluidized bed behavior. This renders the model particularly well-suited for the purpose of computational fluid dynamics (CFD) simulations of gas–solid systems.

2.1.4. Heat transfer model

In this study, the heat transfer model was developed based on an assumption that wall radiation is effectively blocked due to the chaotic movement of particles. Additionally, the heating wall was considered adiabatic, meaning that no heat loss occurs through the wall itself. Under these conditions, the wall-to-bed heat transfer coefficient (hwh) is defined as follows:

$$h_{\mathrm{w}} = \frac{q}{T_{\mathrm{w}} - T_f} = \frac{q}{\frac{1}{H}\int_0^H \Delta \mathrm{T}\ \mathrm{dh}} \qquad (29)$$

where:

- q is the heat flux,
- Tw and Tf indicate the wall and fluid temperatures,
- H is the height of the bed, and
- ΔT represents the temperature difference across the bed.

Gas–Solid Heat Transfer

For heat exchange between the gas and solid phases, the heat transfer coefficient (hgsh) is determined using two widely adopted models:

1. Ranz–Marshall Model [36]

This model estimates the Nusselt number (Nus) for the solid phase using the Reynolds number (Res) and the Prandtl number (Pr):

$$h_{gs} = \frac{k_s Nu_s}{ds} \qquad (30)$$

$$sNu_s = 2.0 + 0.6 Re_s^{0.5} Pr^{1/3} \qquad (31)$$

where

- ksk is the solid-phase thermal conductivity,
- dsdis the solid particle diameter,
- Res represents the solid-phase Reynolds number, and
- Pr is the gas-phase Prandtl number.

2. Gunn Model [37]

The Gunn correlation provides a refined estimation of gas–solid heat transfer for dense fluidized beds and it incorporates corrections for particle concentration effects.

$$h_{gs} = \frac{6 k_g a_s a_g Nu_s}{d_s^2} \qquad (32)$$

$$Nu_s = \left(7 - 10_{ag} + 5a_g^2\right)\left(1 + 0.7 Re_s^{0.2} Pr^{\frac{1}{3}}\right) + \left(1.33 - 2.4_{ag} + 1.2a_g^2\right) + Re_s^{0.7} Pr^{1/3} \qquad (33)$$

where

- kg is the gas thermal conductivity,
- αg and αs are the gas and solid volume fractions, respectively,
- Nu is the solid-phase Nusselt number,
- Res and Pr are the Reynolds and Prandtl numbers, respectively.

Additionally, the Prandtl number is given by:

$$\mathrm{Pr} = \frac{C_{\mathrm{p}\mu\mathrm{g}}}{kg} \qquad (34)$$

The solid-phase Reynolds number is determined as:

$$Re_s = \frac{Pg|\vec{v}\, g - \vec{v}\, s|ds}{\mu_g} \qquad (35)$$

where

- Cp is the gas-phase heat capacity,
- μg is the gas viscosity,
- ρg is the gas density, and
- $\vec{v}g - \vec{v}s$ represents the relative velocity between the gas and solid phases.

2.1.5. Species transport model

To analyze the behavior of reactants within the fluidized bed reactor (FBR), a species transport model is employed to describe mass transfer of substances. The governing equation

for the species transport is expressed as follows:

$$\frac{\partial}{\partial t}(pY_n) + \nabla.(p\vec{v}Y_n) = -\nabla.\vec{J}_n + R_n + S_n \quad (36)$$

where

- Yn indicates the mass fraction of the species n,
- J⃗n is the diffusion flux,
- Rn is the net rate of substance production due to reactions,
- Sn is the source term, which accounts for any external sources or sinks,
- P is the system, and
- v⃗ is the flow velocity vector.

This equation describes the change in the concentration of species over time, considering both the convective transport (due to the flow of the system), diffusion, chemical reactions, and any external influences on the species.

2.2. Chemical reaction kinetic model

In this study, the kinetic model of chemical reactions, developed by Liu et al. [29], was integrated with the Eulerian-granular model (EGM) for simulations. The reactions focused in this study were the hydrogenation and hydrochlorination of $SiCl_4$, each with their own distinct rate expressions.

Hydrogenation Reaction Rate
The rate for the hydrogenation of $SiCl_4$ is expressed as:

$$R_{cl} = k_0 \frac{PS_iCL_4PH_2}{1-\left(\frac{PSiHCL_3}{K_P PSiCL4 P_{H_2}^{\frac{2}{3}}}\right)^{\frac{4}{3}}}\left(1 + K_1 PSiCl_4 + \left(\frac{PSiHCi_3}{PH_2}\right)^{1/3} K_2\right) \quad (37)$$

where

- $PS_iCL_4PH_2$, and $PSiHCL_3$ are the partial pressures of $SiCl_4$, H_2, and $SiHCl_3$ respectively,
- k0 is the apparent rate constant,
- K_p and K_2 are empirical constants that depend on the system.

Hydrochlorination Reaction Rate
Similarly, the rate for the hydrochlorination of $SiCl_4$ follows the equation:

$$R_{c2} = k_0 \frac{PSiCl4PHCl}{1-\left(\frac{PSiHCl_3}{k_P PSiCl_4 P_{H_2}^{1/2} P_{HCl}^{1/2}}\right)^{2/3}}\left(1 + K_1 PSiCl_4 + \left(\frac{PSiHcl_3}{PH_2}\right)^{1/2}\left(\frac{PHCl}{PH_2}\right)^{1/2} K_2\right) \quad (38)$$

where

- $PSiCl4PHCl$, and $PSiHcl_3$ represent the partial pressures of the respective substances involved in the reaction.

Apparent Rate Constant (Arrhenius Expression)
The apparent rate constant for the reactions is described using the Arrhenius equation, which accounts for the temperature dependence of the rate constant:

$$K_0 = A\ exp\left[\frac{E}{R}\left(\frac{1}{T_R} - \frac{1}{T}\right)\right] \quad (39)$$

where

- A is the frequency factor,
- Eis the activation energy,
- R is the universal gas constant,
- Tr and T are the reference and reaction temperatures, respectively.

Reaction Parameters for Species (Kn)
For each species involved in the reaction, the temperature dependence of the reaction rate constants is captured by the following equation:

$$K_m = K_{n,0}\ exp\left[\frac{\Delta H_N}{R}\left(\frac{1}{T_R} - \frac{1}{T}\right)\right], n = p, 1,2 \quad (40)$$

where

- K_n is the pre-exponential factor,
- ΔH_N is the enthalpy change for the reaction,
- Tr and T are the reference and reaction temperatures, respectively.

As outlined in Table 1, the key kinetic parameters govern the reaction dynamics within the system, based on the model proposed by Liu et al. [29]. These parameters play a crucial role in defining reaction rates, adsorption behaviors, and thermodynamic properties.

Table 1. Reaction kinetic parameters

Parameter	Value	Unit	Description
Pre-exponential factor (A)	0.22	mol/(g·s·atm²)	Representing the frequency of molecular collisions leading to a reaction.
Activation energy (E)	77.01	kJ/mol	The minimum energy required for the reaction to proceed.
Reference temperature (Tr)	773	K	The temperature at which kinetic parameters are referenced.
Equilibrium rate constant (K_p)	0.2645	$atm^{-1/3\{-1/3\}-1/3}$	Determining the equilibrium balance between reactants and products.
Adsorption constant (K_1)	0.2141	$atm^{-1\{-1\}-1}$	Defining the adsorption equilibrium of reactant species.
Adsorption constant (K_2)	8.92	atm^{-1}	Representing the adsorption behavior of different reaction components.
Enthalpy change (ΔH_1)	32.45	kJ/mol	Heat change associated with the first reaction step.
Enthalpy change (ΔH_2)	−12.85	kJ/mol	Thermal energy variation in the secondary reaction.
Overall enthalpy change (ΔH_P)	−36.73	kJ/mol	Net enthalpy change of the reaction system.

Key Insights:

- The pre-exponential factor (A) determines how frequently

molecules collide with sufficient energy for a reaction.
- Activation energy (E) sets the energy threshold required for a reaction to occur.
- Equilibrium and adsorption constants (K_p, K_1, K_2) define how reactants and intermediates interact under specific process conditions.
- Enthalpy changes (ΔH_1, ΔH_2, ΔH_P) indicate the heat absorption or release associated with each reaction step, which is critical for thermodynamic balance.

2.3. Numerical solution algorithms

In this study, numerical simulations were conducted using ANSYS FLUENT 16.1, a well-established computational fluid dynamics (CFD) software widely utilized for modeling multiphase flow and chemical reaction systems. To ensure a high degree of accuracy in capturing the fluidization behavior and gas-solid interactions within the fluidized bed reactor (FBR), the computational domain was carefully discretized into a structured mesh consisting of 24,000 grid cells. This mesh was generated using the ANSYS Mesh 16.1 pre-processing module, which enabled precise control over cell size, aspect ratio, and overall grid quality, ensuring a balance between computational efficiency and numerical resolution. To solve the governing equations governing momentum, energy, and mass transfer phenomena within the system, the Semi-Implicit Method for Pressure-Linked Equations (SIMPLE) algorithm was employed. This algorithm has been shown to be particularly effective in handling pressure-velocity coupling, which is essential for accurately resolving the fluidization dynamics in an Eulerian-granular framework. s, the SIMPLE algorithm enhances the stability and convergence of the numerical solution by iteratively refining pressure and velocity correction, thereby reducing errors associated with pressure-gradient-driven flows.

To discretize the spatial derivatives of the governing equations, a first-order upwind scheme was applied. This scheme ensures numerical stability by approximating the convective fluxes based on the flow direction, thereby reducing the risk of oscillations and divergence. Despite the potential of higher-order schemes, such as second-order upwind or QUICK (Quadratic Upstream Interpolation for Convective Kinematics), to enhance accuracy, the first-order upwind approach was selected for its robustness in managing sharp gradients commonly observed in fluidized bed reactors. Additionally, the simulation framework incorporated was integrated with well-defined boundary conditions to reflect the actual operational characteristics of the system. At the inlet, a velocity inlet boundary condition was imposed, ensuring a controlled gas-phase flow rate that drives the fluidization process. At the outlet, the application of a pressure outlet boundary condition was imperative to maintain a stable pressure gradient to facilitate mass transport. Additionally, the enforcement of a no-slip boundary condition was essential. This ensured that enforced on the reactor walls for both the gas and solid phases. This ensured that gas molecules and solid particles adhered to the walls without penetration or slip, thereby replicating realistic wall-fluid interactions.

To enhance the accuracy of the numerical model, it was necessary to define and validate the key operational parameters and boundary conditions. These configurations, including gas velocity, particle properties, and temperature conditions, are summarized in Tables 2 and 3, This ensures that the simulation results align with experimental and theoretical expectations. The numerical setup, which has been carefully structured, provides a robust foundation for analyzing fluidization behavior, reaction kinetics, and heat transfer dynamics within the $SiCl_4$ hydrochlorination process. This, in turn, ultimately contributes to the optimization of fluidized bed reactor performance.

Table 2. Detailed process parameter specifications

Parameter Description	Value & Unit
Height of the Bed	1.22 m
Width of the Bed	0.1524 m
Density of the Solid Material	2330 kg/m³
Diameter of Solid Particles	235 µm
Coefficient of Restitution (Solid–Solid Collisions)	0.9 (dimensionless)
Density of the Gas Phase	1.225 kg/m³
Dynamic Viscosity of the Gas	1.72 µPa·s
Initial Bed Height	0.60 m
Initial Solid Volume Fraction	0.60 (dimensionless)
Gas Inlet Velocity	0.10, 0.30, and 0.50 m/s (depending on this work)
Temperature of the Reactor Wall	773 K
Temperature at the Gas Inlet	300 K
Operating Pressure	2.0 MPa
Molar Ratio of $SiCl_4$: H_2 : HCl	1 : 4 : 1

Table 3. Simulation boundary condition specifications

Boundary Condition Parameter	Specification / Value
Inlet Condition	Velocity Inlet
Outlet Condition	Pressure Outlet
Drag Force Model	Syamlal-obrien [35]
Heat Transfer Model	Guun [37]
Granular Viscosity Model	Gidaspow et al. [35]
Granular Bulk Viscosity Model	Lun et al. [32]
Particle Restitution Coefficient	0.9
Wall Boundary Condition	No-slip
Friction Viscosity Model	Schaeffer [33]

2.4. Geometrical configuration

In this study, the geometric model of the Fluidized Bed Reactor (FBR) was developed based on the prototype described in reference [38], ensuring consistency with previous experimental and theoretical investigations. The reactor system comprised several essential components, including a reactant metering and delivery system, the fluidization chamber, and an instrumentation setup for pressure signal acquisition. Fig. 1 depicts a detailed schematic representation of the reactor's structural design, along with its computational mesh

configuration. Meanwhile, Table 2 presents a comprehensive summary of the geometric parameters employed in the numerical simulation. The fluidized bed reactor was designed as a vertically oriented cylindrical column, standing at an overall height of 1.22 meters. The fluidization zone, where the reactant gases interacted with solid silicon particles, had an internal diameter of 0.1524 meters. Furthermore, the reactant gases, specifically silicon tetrachloride ($SiCl_4$), hydrogen (H_2), and hydrogen chloride (HCl), were introduced into the reactor through an inlet distributor positioned at the base of the column. This gas-phase injection plays a critical role in initiating and sustaining fluidization, ensuring homogeneous mixing between silicon particles and the reactive gas flow. The chemical reactions took place within the fluidized zone, after which the resultant exhaust gases exited the reactor system through a designated outlet at the top.

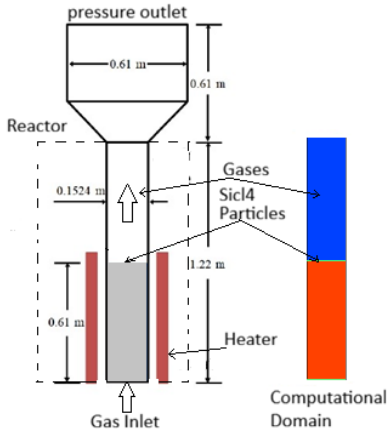

Fig. 1. Diagram of the geometric model and computational domain for the experimental FBR prototype by Hsu et al.

Given the computational demands associated with simulating a three-dimensional (3D) FBR system, a geometrical simplification was implemented to enhance computational efficiency without compromising the accuracy of the results. Instead of modeling the entire 3D cylindrical structure, the reactor was transformed into a two-dimensional (2D) axisymmetric representation. This is a commonly employed approach in CFD-based reactor simulations, and this simplification significantly reduces computational load, allowing for higher mesh resolution and more refined numerical analysis. It also maintains the fundamental fluidization dynamics and reaction characteristics of the system.

The selection of boundary conditions was also critical in defining the flow characteristics within the reactor. At the inlet, a uniform velocity boundary condition was applied, ensuring a consistent gas-phase entry profile. A pressure outlet condition was applied to the outlet boundary, which maintained an appropriate pressure gradient for gas-phase transport. Additionally, a no-slip wall boundary condition was enforced along the reactor walls, dictating that both gas and solid phases adhere to the reactor's internal surfaces. This accurately represents realistic wall-fluid interactions. The numerical model developed for this study provides a rigorous framework for analyzing fluidization behavior, chemical reaction performance, and heat transfer dynamics within an $SiCl_4$ hydrochlorination process.

2.5. Grid independence verification

To verify computational accuracy, a grid independence test was conducted using three distinct mesh configurations with 15,000, 24,000, and 42,000 factors, respectively. Fig. 2(a) exhibits the pressure drop analysis and Fig. 2 shows the influences of the grid size on the simulation results, where the of the mean solid volume fraction was simulated at gas inlet velocity of 0.1 m/s. It can be seen that the profiles of mean solid volume fraction were nearly identical for grid meshes of 24,000 and 42,000 elements, while a noticeable deviation appeared with the coarse 15,000 grids. It indicated that the grid meshes of 24,000 and 42,000 elements was considered sufficiently fine for reliable simulations and the coarse grid mesh of 15,000 element might lead to discrepancies. It was found that the grid mesh of 24,000 element was sufficient for the numerical simulations. As a result, this mesh configuration was selected for further evaluation, as it offered a foremost combination of computational accuracy and performance.

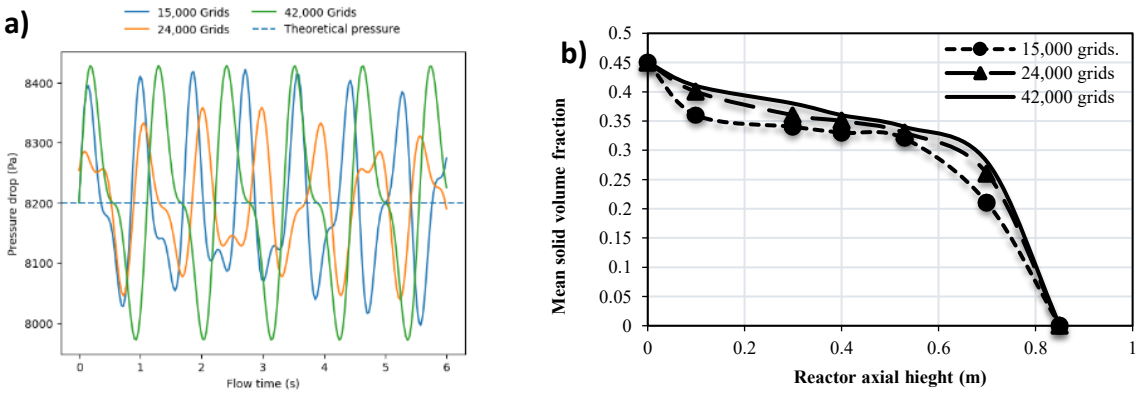

Fig. 2. (a) Pressure Drop Analysis. (b) Influences of grid mesh on simulation results of the mean solid volume fraction at gas inlet velocity of 0.15 m/s

3. Results and Discussion

3.1. Model validation

The model was validated through the examination of the gas temperature distribution within the reactor and comparison with experimental temperature profile, as depicted in Fig. 3(a). This is contradicting to the simulation outcomes in opposition to values derived from empirical correlations, as illustrated in Fig. 3(a). The particular empirical formulation utilized for

evaluation, sourced from references [39], is distinctive in Table 4 (the minimal fluidization speed (Umf), the minimum bubbling velocity (Umb), the minimum slugging speed (Ums), minimum fluidization (Hmf), the maximum mattress growth peak (Hmax), the Reynolds number at minimum fluidization (Remf), and the bed voidage at minimal fluidization (αmf)). As depicted in Fig. 3(a), the EGM-predicted values for Hmax demonstrated an almost linear increase with rising inlet fuel velocities. When the inlet velocity was set to 0.1 m/s, 0.30 m/s, and 0.50 m/s, the discrepancies among the simulated Hmax values and human- computed using empirical correlations were restricted to 2%, 4%, 6%, and 8%, respectively. These deviations fall within an acceptable variety, thereby reinforcing the EGM's capacity to accurately predict bed enlargement dynamics. The minimal percentage errors further substantiated the robustness of the numerical version in capturing key hydrodynamic characteristics in the FBR.

Besides bed expansion analysis, the model was validated through the examination of the gas temperature distribution within the reactor and comparison with experimental temperature profiles, as depicted in Fig. 3(b). The experimental dataset, obtained from the work of Hsu [38], provides a comprehensive benchmark for evaluating the EGM's predictive accuracy. In the experimental configuration, the gas was introduced at an inlet temperature of 300 K, with the reactor walls maintained at 923 K. An inlet velocity equal to five times the minimum fluidization velocity (U/Umf=5U/U_{mf} = 5U/Umf=5), was used to ensuring uniform fluidization conditions. The simulated temperature profile closely followed the experimentally measured trend, demonstrating a sharp temperature rise from approximately 400 K to 910 K as the gas flowed through the fluidized bed. The rapid temperature escalation observed in both the numerical and experimental results highlights the efficient heat transfer mechanisms within the FBR. Furthermore, the strong agreement between the simulated and experimental data confirms the validity of the EGM.

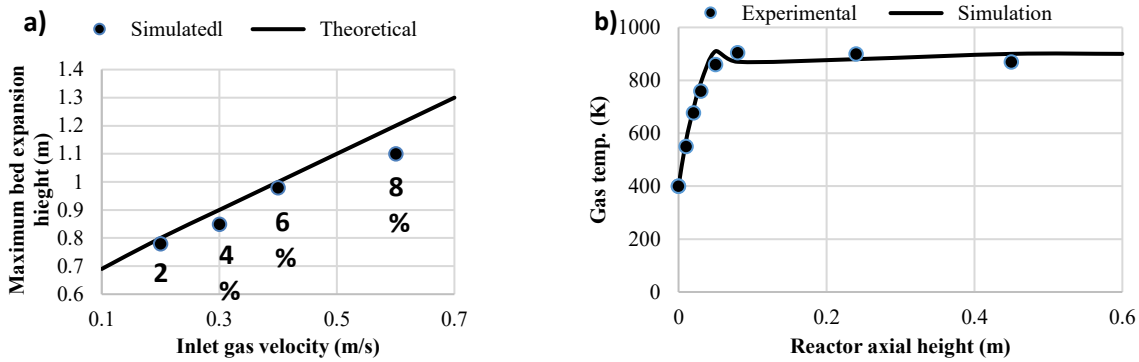

Fig. 3. Validation of the computational model

Table 4. Empirical formulas for fluidization characteristics parameters [39,40]

Parameters	Formulas
Umf	$Umf = Remf \frac{\{\mu_g\}}{\{\rho_g d_s\}}$ (41)
Umb	$Umb = 0.35\,\rho_g D$ (42)
Ums	$Ums = Umf\,\rho_g D + 1.6 \times 10^{\{-5\}}\left(60 \times (100D)^{\{0.175\}} - 100\,H_{\{mf\}}\right)^2$ (43)
Hmf	$Hmf = Hmf = \frac{\{H(1-\alpha)\}}{\{(1-\alpha_{\{mf\}})\}}$(44)
ΔP	$\Delta P = Hmf\left(1 - \alpha_{\{mf\}}\right)\left(\rho_s - \rho_g\right)g$ (45)
Hmax	$Hmax = = Hmf + Hmf \times \frac{\{U - Umf\}}{\{0.5\sqrt{\{gD\}}\}}$(44)

The observed level of $SiCl_4$ conversion can be explained by the balance between reaction kinetics and gas–solid mass-transfer limitations, as revealed by the validated EGM results. Although higher inlet gas velocities have been shown to enhance mixing and heat transfer, the accompanying increase in bed voidage and bubble fraction has been demonstrated to reduce effective gas–solid contact time. As a result, the system underwent a gradual transition from a kinetically controlled regime to one dominated by external film and intra-particle mass-transfer resistance, resulting in the conversion to plateau rather than a continuous increase. This behavior indicates that the effective Damköhler number decreases with rising velocity, confirming that mass-transfer constraints, not reaction temperature, ultimately limit the achievable $SiCl_4$ conversion under the studied conditions.

In addition to validating temperature profile, further steps were taken to support the predictive competence of the Eulerian–Granular Model (EGM) by comparing its behavior trends with well-established observations reported in the literature. For instance, in the context of studies of fluidized-bed reactors characterized with heterogeneous gas–solid reactions, the utilization of validated CFD or reactor-flow models frequently entails the benchmarking of not only hydrodynamics and thermal behavior but also product distribution and conversion behavior against both experimental data and literature reports [40]. In a particular study on dehydrogenation in a fluidized bed, the authors successfully reproduced both flow patterns and reaction rates with relative deviations of less than 10–26% in comparison to experimental plant data [41]. It is demonstrated from the observation that the EGM predicts $SiCl_4$ conversion behavior that qualitatively matches the regime-dependent trends. This is evidenced by higher conversion under bubbling conditions and reduced conversion in slugging or low-velocity regimes. The model is thus shown to deliver credible chemical-performance predictions. Therefore, while direct comparison of conversion with experimental data remains limited by a paucity of

published $SiCl_4$-specific data, the consistent flow and thermal validation results, in conjunction with the congruence of predicted trends with general fluidized-bed reaction behavior as documented in the literature, serve to reinforce the reliability of our model's reaction predictions.

3.2. Flow pattern and regime

Fig. 4 illustrates the distribution of solid volume fraction for various inlet gas velocities. This facilitates an in-depth angle of the conduct of the fluidized mattresses under unique running situations. It is vital to observe that this evaluation exclusively examines the hydrodynamic behavior of the fluidized bed, without incorporating any chemical reaction results. At an inlet speed of 0.10 m/s (see Fig. 4(a)), the flow rate of inlet gasoline is equivalent to 0.10 m/s, near the theoretical minimum fluidization speed (Umf) of zero. A solitary bubble emerges from the center of the mattress and ascends regularly before ultimately dissipating. Following a brief phase of growth, the top of the mattress stabilizes, exhibiting minimal fluctuations. As demonstrated in Fig. 4(b), an increase in the inlet fuel speed to 0.30 m/s approaching the theoretical minimum bubbling speed (Umb) of 0.26 m/s, results in an enhancement of turbulent conduct of the stable phase. In this condition, the formation of small, dense bubbles begin at the base of the mattress, whilst large, semi-circular bubbles appear in proximity to the partitions. The diameter of bubble reaches approximately 0.6 times the diameter of the bed, signaling that the system is transitioning into a state of effervescence. At an inlet gas speed of 0.50 m/s (see Fig. 4(c)), near the theoretical minimal slugging velocity (Ums) of zero.69 m/s, the movement of the solid debris becomes substantially more vigorous. In this instance, the bubbles initially formed at the base of the bed disappear. Instead, the layers of bubbles emerge within the middle of the mattress, indicating a transition to a slugging regime. These detailed observations confirm that the developed Eulerian Granular Model (EGM) is capable of effectively capturing the alterations in flow patterns as gas velocities increase, accurately describing the transition from fluidization to bubbling and finally to slugging.

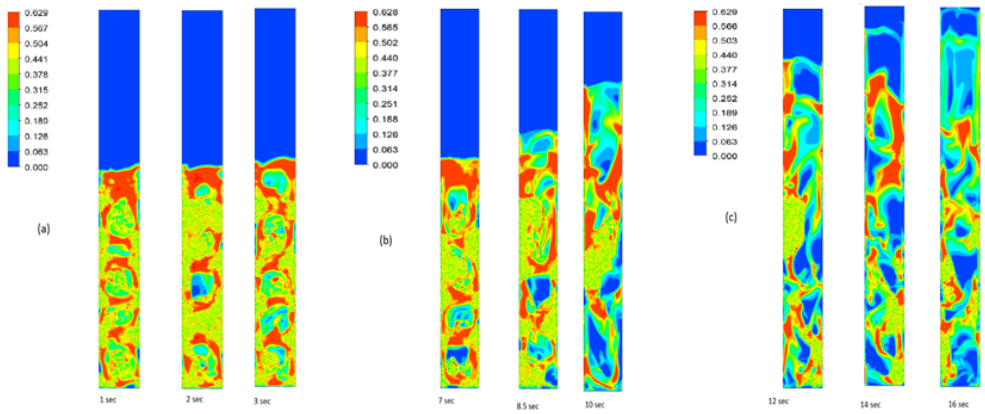

Fig. 4. Solid volume fraction distribution at different inlet gas velocities (without chemical reactions)

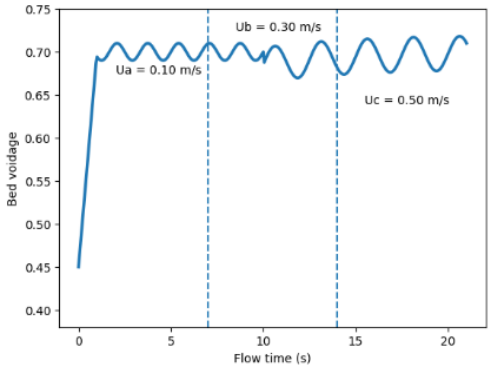

Fig. 5. Illustrates the temporal variant of mattress void age at special inlet gasoline velocities

Fig. 5 illustrates the temporal variant of bed void age at specific inlet gasoline velocities. At an inlet pace of 0.10 m/s, the bed void age started off evolved at 0.45 and rises to 0.70 within the initial second. The void age oscillated around 0.70 between 1 and 10 seconds. At this stage, the fluidization behavior of the bed remained notably diffused, with a single "bubble" forming in the middle (as depicted in Fig. 4(a)). When the inlet gasoline speed was elevated to 0.30 m/s, the bed entered the bubbling kingdom (see Fig. 4(b)). In this instance, particle motion turned into increasingly chaotic, highly determined by the fluctuation of the bubbles. As the process of coalesce occurs, the void age increases, whereas a decrease occurs during the collapse of bubbles. A similar increase in inlet pace to 0.50 m/s resulted in the mattress transitioning into the slugging nation (see Fig. 4(c)). In this regime, the formation and breakup of bubbles was more frequent occurrence. The presence of bubble-cutting layers within the mattress led to an unexpected increase in the void age to about zero.

The temporal evolution of bed voidage under different inlet gas velocities also influences mass transfer and reaction performance. At low velocities (0.50 m/s), the loosely fluidized bed and the limited activity of bubble result in restriction to gas–solid contact, resulting in the formation of mass-transfer-limited reaction zones. As the velocity increases to 0.30 m/s, the onset of bubbling enhances mixing and local gas–solid interactions, thereby reducing mass-transfer constraints. At a velocity of 0.65 m/s, the slugging regime generates large, transient bubbles and an uneven voidage distribution. This can result in the formation of regions demonstrating insufficient contact, despite the enhancement of overall circulation. These observations indicate a direct correlation between fluidization regime transitions and the extent of mass-transfer limitation, thereby ultimately setting the practical reaction limits for $SiCl_4$

conversion.

Fig. 6 illustrates the mean mass fraction distribution of $SiCl_4$ for various inlet gas velocities. In the case of decreased velocities of gasoline, the drag pressure exerted by rising gasoline marginally exceeded the gravitational pressure performing on the debris. Consequently, $SiCl_4$ predominantly accumulated in the middle and lower sections of the mattress. When the inlet gas velocity reached 0.30 m/s, the bed entered the bubbling phase. As the gas pace continued to increase to 0.65 m/s, the bed entered a state of slugging. In this state, the $SiCl_4$ gasoline, in conjunction with the solid particles, exited the mattress, thereby leading to a reduction in the $SiCl_4$ concentration within the upper areas.

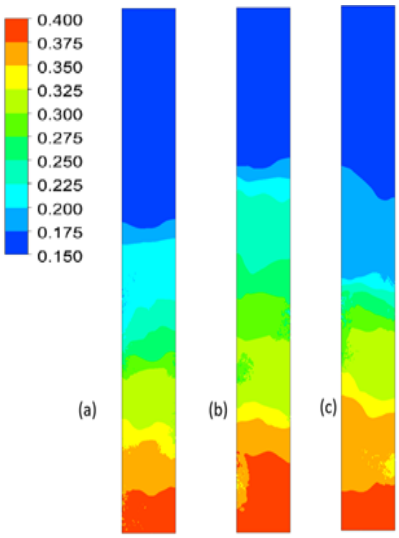

Fig. 6. Variation of the average mass fraction of SiCl4 at different inlet gas velocities. (a) Ua = 0.10 m/s; (b) Ub = 0.30 m/s; (c) Uc = 0.50 m/s

3.3. Heat transfer characteristics

In this investigation, separate heat transfer models—Guun's version and the Ranz–Marshall model—was applied to estimate the gas–strong heat switch coefficient in the fluidized bed reactor (FBR). As illustrated in Fig. 7, the axial distribution of the gas–stable warmth switch coefficients as expected via each fashion, in conjunction with the corresponding stable Reynolds number (Re_s). The findings of this study demonstrated a robust correlation between variations in the heat switch coefficient and Re_s. Guun's version has been shown to consistently predict better warmness switch coefficients in comparison to the Ranz–Marshall model. This divergence can be attributed to the foundational differences of their theoretical strategies:

- Ranz–Marshall Model: This model was originally developed for the study of isolated spherical particles in a fluid. It tends to underestimate the warmth transfer in dense fluidized structures. The reason for this is that frequent particle collisions and interactions appreciably increase the overall warmth alternate.
- Guun's Model: This model consists of the collective consequences of particle clustering and interphase interactions, rendering it particularly suitable for the dense-phase fluidization scenarios observed in FBRs.

Fig. 8 provides further insights into the reactor's thermal performance by displaying the axial temperature profiles of the gas phase along the reactor's height. At an axial height of Z = 0.1 cm, the average gas temperature in the bed was almost equal to the inlet temperature, approximately 400 K. As the gas ascended, its temperature increased steadily, reaching approximately 680 K at Z = 0.5 cm. At a distance of 1 cm from the center, a more pronounced temperature rise was observed, with the gas temperature rising to almost 710 K, approaching the temperature of the reactor wall. These observations emphasize the high efficiency of heat transfer within the fluidized bed, as demonstrated by the rapid thermal equilibration between the gas and solid phases. Notably, the system reaches near thermal equilibrium with the reactor walls over an axial distance of a mere 13 mm.

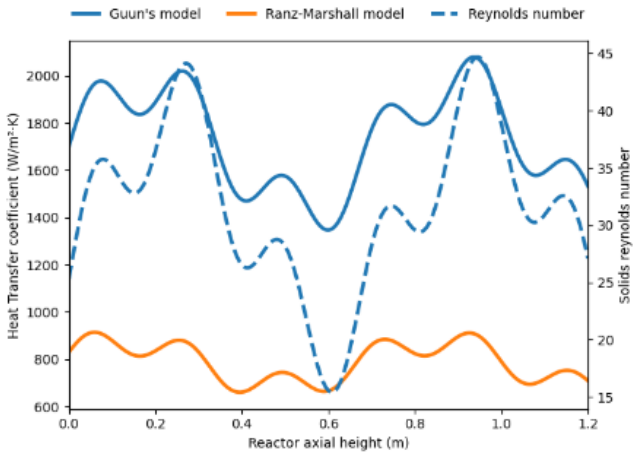

Fig. 7. Comparison of simulated gas-solid heat transfer coefficients using different heat transfer models based on predicted solid reynolds number

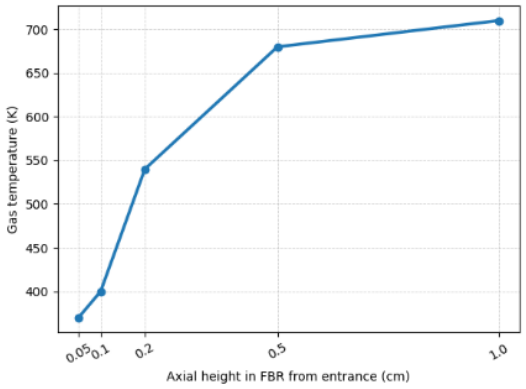

Fig. 8. Predicted axial gas temperature distribution in FBR at the inlet (Ub = 0.30 m/s)

3.4. Chemical reaction performance

As illustrated in Fig. 9, the estimation of the strong extent fraction was made at specific inlet fuel velocities. This estimation was made with consideration for the interaction of go with the flow dynamics, warmth switch, and chemical reactions. As demonstrated in Fig. 9(a), when the inlet gasoline pace was set to 0.10 m/s, a single small bubble appeared in the bed, and the overall apparatus remained relatively stable with minimal disturbance. This observation indicated that, at this stage, the $SiCl_4$ hydrochlorination reaction was predominantly constrained to the lower and significant regions of the bed. As the inlet fuel velocity increased to 0.30 m/s, the bed expanded,

transitioning into an effervescent regime. In this phase, the formation and circulation of bubbles enhanced the combination of $SiCl_4$ gas with silicon particles, particularly in the center and upper sections of the reactor, promoting a greater uniform response environment. When the inlet gas velocity was further raised to 0.50 m/s, the intensified gas flow led to increased fluidization, causing particles to rise more rapidly. Some particles were carried to the upper level of the bed with the potential to be entrained out of the reactor. In this slugging regime, the accumulation of large bubbles significantly increased bed voidage, thereby reducing effective gas–solid interactions.

The CFD simulations incorporating $SiCl_4$ kinetics revealed that chemical conversion was highly determined by the fluidization regime. At low inlet velocity (0.10 m/s), the restriction of bubble formation limited gas–solid contact, thereby confining the reaction to the lower and denser regions of the bed. In the bubbling regime (0.30 m/s), enhanced mixing and bubble circulation promoted more uniform contact between $SiCl_4$ and silicon particles, increasing reaction efficiency. However, at higher velocities (0.50 m/s), slugging and particle entrainment lead to excessive voidage and reduced gas–solid interactions, limiting conversion despite vigorous fluidization. The findings of this study suggest that optimal chemical performance occurs in the bubbling regime, where mass-transfer and mixing are balanced, while both low and high velocities imposed practical.

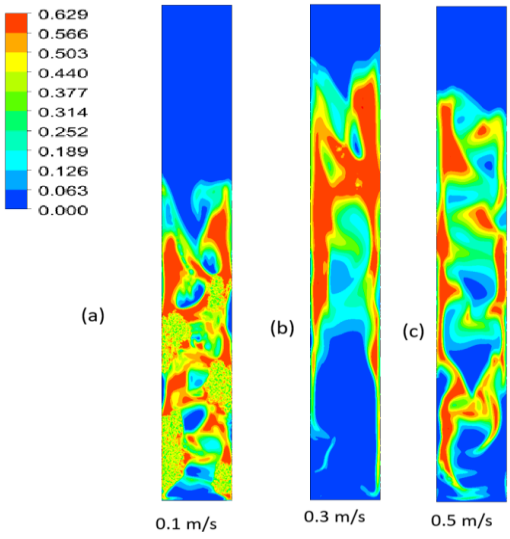

Fig. 9. Predicted solid volume fraction in $SiCl_4$ Hydrochlorination Under Different Inlet Gas Velocities (Including Chemical Reactions): (a) Ua = 0.10 m/s; (b) Ub = 0.30 m/s; (c) Uc = 0.50 m/s

Fig. 9 also illustrates the predicted solid volume fraction during the hydrochlorination of $SiCl_4$ under varying inlet gas velocities and the chemical reactions. At a low gas velocity of 0.10 m/s (see Fig. 9(a)), the bed operated near the minimum fluidization velocity (Umf), resulting in a relatively stable and static bed with minimal fluidization. In this state, the solid particles were loosely packed, and merely a single small bubble formed at the center of the bed. The limited fluidization hindered the mixing of $SiCl_4$ gas with the solid silicon particles, causing the reaction to primarily occur in the lower and middle sections of the bed. Consequently, the distribution of the reaction product, $SiHCl_3$, was concentrated in these regions, with an average mass fraction of approximately 8.21%. When the gas velocity was increased to 0.30 m/s (see Fig. 9(b)), the bed transitions into the bubbling fluidization regime. In this phase, the formation of multiple bubbles enhanced the mixing of the gas and solid phases, leading to a more uniform distribution of reactants and products throughout the bed. This resulted in a higher mass fraction of $SiHCl_3$, which peaked at 14.01%. The bubbling regime was thus identified as the optimal condition for maximizing reaction efficiency.

However, when the gas velocity was further increased to 0.50 m/s (see Fig. 9(c)), the system entered the slugging regime. In this phase, the gas flow became more intense, causing large bubbles to form and rise rapidly through the bed, thereby leading to the formation of bubble cutoff layers in the middle of the bed, where gas and solid interactions were disrupted. Consequently, $SiCl_4$ was carried quickly to the upper of the bed, reducing the residence time available for the gas to react with the solid particles. The reduced contact time between the reactants negatively impacted the reaction efficiency, causing the mass fraction of $SiHCl_3$ to drop to 10.07%.

Fig. 10 provides a complementary analysis, illustrating the distribution of the mass fraction of $SiHCl_3$ produced during the hydrochlorination process at varying gas velocities. At a gas velocity of 0.10 m/s, the distribution of $SiHCl_3$ was predominantly found in the lower and middle sections of the bed, reflecting the limited fluidization and mixing in the minimum fluidization state. However, as the gas velocity increased to 0.30 m/s, the distribution of $SiHCl_3$ became more uniform across the bed, particularly in the middle and upper regions, due to the enhanced mixing in the bubbling regime. This uniformity is crucial for achieving high conversion rates and optimal reaction conditions. However, at 0.50 m/s, the accelerated movement of gas and solids to the upper sections of the bed resulted in a reduce of the concentration of $SiHCl_3$ concentration. This was due to the inadequate gas residence time hindering the completion of reaction.

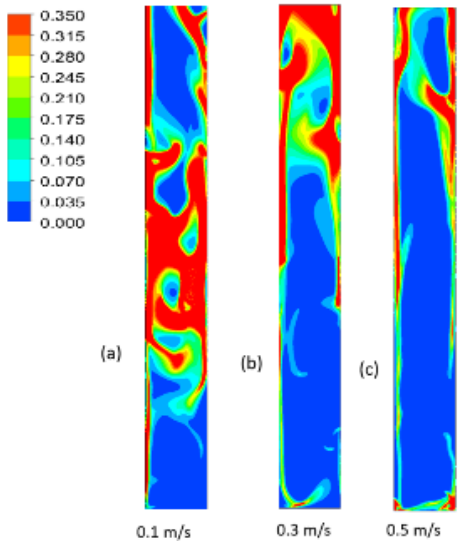

Fig. 10. Distribution of SiHCl3 product mass fraction at varying inlet gas velocities with chemical reactions (a) Ua = 0.10 m/s; (b) Ub = 0.30 m/s; (c) Uc = 0.50 m/s

The study demonstrated that the bubbling regime at a gas velocity of 0.30 m/s provided the optimal conditions for the hydrochlorination of $SiCl_4$, offering a balance between

effective fluidization, optimal mixing, and sufficient residence time for the reaction to proceed efficiently. The findings highlight the critical role of fluidization behavior in determining the performance of chemical reactions in fluidized bed reactors, with implications for optimizing industrial-scale processes.

Fig. 11 illustrates the conversion rates of both $SiCl_4$ hydrogenation and hydrochlorination reactions (Eq. 1 and 2) at different inlet velocities. The highest conversion rate was observed when the system was in the bubbling phase, where gas and solids were well-mixed, thus promoting a more efficient $SiCl_4$ conversion. The predicted rate reached 28.84% under the bubbling conditions as noted in previous studies [27,28].

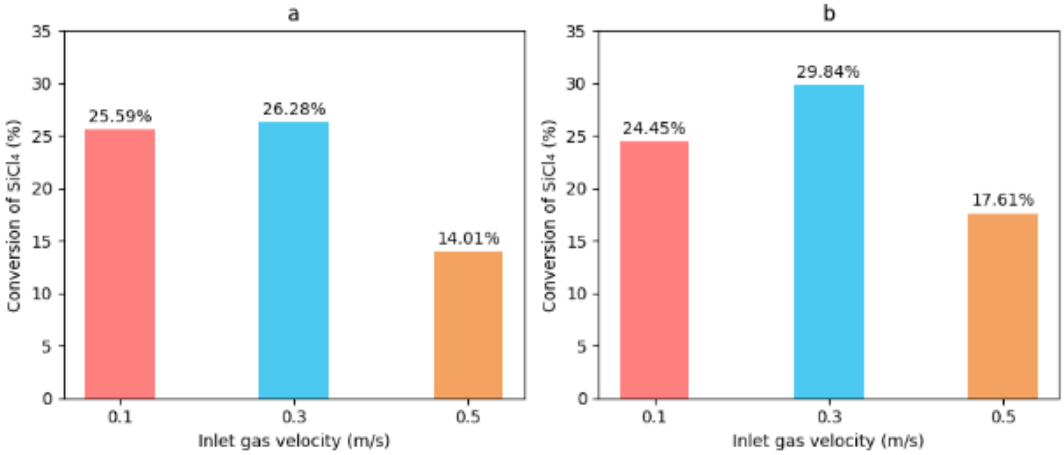

Fig. 11. Effect of inlet gas velocities on SiCl4 conversion: (a) Hydrogenation process; (b) Hydrochlorination process

3.5. Discussion

In this research, the EULERIAN -Granular Model (EGM) results demonstrated that the model was able to capture dynamic alterations in the flow patterns. including the transition from the phase of dilution phase to the bubble stage, followed by the slugging phase, with a high degree of accuracy in predicting the height of the prescription layer (HMAX) and its distributing. The gas heat has been verified by the accuracy of the model by comparing the calculated values of the height of the luminous layer (HMAX) with theoretical values derived from experimental formulas. The results demonstrated that the model predicts a semi-written increase in HMAX with an increase in gas speed, with slight differences ranging from 1% to 9% in comparison to experimental values. These results enhanced the reliability of the model in predicting the behavior of the tall layer under different operating conditions. Furthermore, the distribution of gas temperature as calculated with the experimental data from the HSU study (38) was compared with the model, which showed a strong compatibility with the experimental data. This confirms the model's ability to capture thermal gradients and the efficiency of heat transfer within the reactor and regarding previous studies. Regarding heat transfer, the research demonstrated that the Gun Form is a predictor of elevated heat transmission.

Regarding the performance of the chemical reaction, the research demonstrated that the highest transformation rate $SiCl_4$ occurred in the bubble stage, where the confusion between gas and particles was at its peak. This study provides a comprehensive understanding of the complex interactions between hydraulic dynamics, heat transfer, and chemical reaction performance in the luminous layer reactors. By comparing the results with previous studies, it has been emphasized that the model used in this research was able to accurately predict the behavior of the luminous layer under different operating conditions. These results contribute to improving reactor design and operating strategies, which enhances the efficiency of conversion and the stability of operations in the production of $SIHCL_3$.

4. Conclusion

This study presents a comprehensive investigation of the fluidization behavior and chemical reaction performance of $SiCl_4$ hydrochlorination within a fluidized bed reactor (FBR) using an advanced Eulerian–Granular Model (EGM). The results revealed a progressive increase in bed voidage over time, which was closely linked to the evolution of the flow regime within the reactor. This observation highlights the dynamic interaction between gas and solid phases and its impact on the overall fluidization quality and reaction efficiency. As the gas velocity increased, the fluidization quality improved, resulting in a more homogeneous distribution of $SiCl_4$ throughout the reactor bed. The most significant enhancement was observed during the bubbling fluidization stage, where uniform reactant dispersion facilitated superior mass transfer and optimized reaction kinetics. An analysis of heat transfer revealed high level of thermal efficiency within the system. In addition, it was determined that the reaction gases reached the target operating temperature within a distance of 13 mm from the reactor inlet. This rapid thermal equilibration was further supported by the continuous circulation of bubbles, which promoted effective mixing of $SiCl_4$ with silicon particles, thereby increasing the interaction between reactant gases and solids and improving overall reaction conversion efficiency. During the bubbling phase, gas-solid mixing reached its peak, creating optimal conditions for $SiCl_4$ hydrochlorination. The simulation results under these conditions demonstrated a $SiCl_4$ conversion rate of 29.84% and a peak $SiHCl_3$ concentration of 14.01%. These findings underscore the pivotal role of fluidization behavior in maximizing reaction efficiency. Overall, the research provides a detailed understanding of the interplay between hydrodynamics, heat transfer, and chemical reactions in FBRs.

The insights gained can guide the optimization of industrial-scale $SiCl_4$ hydrochlorination processes, improving reactor design, operational strategies, conversion efficiency, and process stability in the production of high-purity $SiHCl_3$.

Recommendations

Based on the findings of the study, several recommendations are proposed to enhance the performance of fluidized bed reactors (FBRs) in the $SiCl_4$ hydrochlorination process. The design of reactor can be enhanced with the incorporation of more efficient gas distributors for the uniform distribution of $SiCl_4$, accurate gas control systems to maintain the bubbling phase, and improved heat transfer through optimized thermal exchangers or high-conductivity materials. To determine optimal conditions, it is important to study the effect of silicon particle size and reactant concentrations on reaction efficiency. Also, in modeling and simulation, the development and validation of more accurate models accounting for particle distribution, viscosity, and varying operating conditions is critical. These models should be subjected to experimental validation through rigorous experimentation with advanced data analysis applied to extract deeper insights. At the industrial level, the adoption of simulation techniques, training of technical staff, and potential integration of AI and machine learning algorithms can facilitate the prediction of reactor performance and optimization of large-scale production processes. These recommendations aim to enhance reaction efficiency, product quality, and provide a foundation for future research and industrial applications.

References

1. M.K.H. Rabaia, C. Semeraro, A.G. Olabi, *Recent progress towards photovoltaics' circular economy*, J. Clean. Prod. 373 (2022) 133864.
2. R. Deng, Y.T. Zhuo, Y.S. Shen, *Recent progress in silicon photovoltaic module recycling processes*, Resour. Conserv. Recycl. 187 (2022) 106612.
3. S. Yadav, K. Chattopadhyay, C.V. Singh, *Solar grade silicon production: A review of kinetic, thermodynamic and fluid dynamics based continuum scale modeling*, Renew. Sustain. Energy Rev. 78 (2017) 1288–1314.
4. Z.F. Nie, Y.J. Wang, C. Wang, Q.J. Guo, Y.Q. Hou, P.A. Ramachandran, G. Xie, *Mathematical model and energy efficiency analysis of Siemens reactor with a quartz ceramic lining*, Appl. Therm. Eng. 199 (2021) 117522.
5. T. Zhou, L.L. Gong, X.D. Cheng, Y.L. Pan, C.C. Li, H.P. Zhang, *Preparation and characterization of silica aerogels from by-product silicon tetrachloride under ambient pressure drying*, J. Non-Cryst. Solids 499 (2018) 387–393.
6. W.J. Ding, J.M. Yan, W.D. Xiao, *Hydrogenation of silicon tetrachloride in the presence of silicon: Thermodynamic and experimental investigation*, Ind. Eng. Chem. Res. 53 (2014) 10943–10953.
7. W.J. Ding, Z.B. Wang, J.M. Yan, W.D. Xiao, *CuCl-catalyzed hydrogenation of silicon tetrachloride in the presence of silicon: Mechanism and kinetic modeling*, Ind. Eng. Chem. Res. 53 (2014) 16725–16735.
8. J. Wu, Z. Chen, W. Ma, Y. Dai, *Thermodynamic estimation of silicon tetrachloride to trichlorosilane by a low-temperature hydrogenation technique*, Silicon 9 (2017) 69–75.
9. Y. Wang, Z. Nie, Q. Guo, Y. Song, L. Liu, *Adsorption behaviors of chlorosilanes, HCl, and H_2 on the Si(100) surface: A first-principles study*, ACS Omega 7 (2022) 42105–42114.
10. S. Ravasio, M. Maso, C. Cavalloti, *Analysis of the gas phase reactivity of chlorosilanes*, J. Phys. Chem. A 117 (2013) 5221–5231.
11. J.Y. Lee, W.H. Lee, Y.K. Park, H.Y. Kim, N.Y. Kang, K.B. Yoon, W.C. Choi, O.B. Yang, *Catalytic conversion of silicon tetrachloride to trichlorosilane for a poly-Si process*, Sol. Energy Mater. Sol. Cells 105 (2012) 142–147.
12. M.P. Jain, D. Sathiyamoorthy, V.G. Rao, *Studies on hydrochlorination of silicon in a fluidized bed reactor*, Indian Chem. Eng. 53 (2010) 61–67.
13. F. Becker, S. Buchholz, L. Mleczko, *Kinetic modeling of the hydrochlorination of silicon with $SiCl_4$ and H_2*, Chem. Eng. Technol. 73 (2001) 686.
14. G.Q. Guan, C. Fushimi, A. Tsutsumi, *Prediction of flow behavior of the riser in a novel high solids flux circulating fluidized bed*, Chem. Eng. J. 164 (2010) 221–229.
15. Q. Wu, S. Wang, K. Zhang, Y.H. Zhao, Y.R. He, *Numerical studies of gas-solid flow behaviors and wall wear in a swirling fluidized bed*, Powder Technol. 388 (2021) 233–240.
16. J. Humadi, E. Rasheed, *Numerical Study of Sodium Bicarbonate Production in Industrial Bubble Columns*, J. Chem. Pet. Eng. 58 (2024) 391–406.
17. Y. Pottimurthy, D.W. Wang, C. Park, S. Patil, A. Tong, L.S. Fan, *Three-dimensional dynamic characterization of square-nosed slugging phenomena in a fluidized bed*, Particuology 67 (2022) 35–46.
18. S.S. Liu, W.D. Xiao, *Numerical simulations of particle growth in a silicon-CVD fluidized bed reactor via a CFD–PBM model*, Chem. Eng. Sci. 111 (2014) 112–125.
19. S.S. Liu, W.D. Xiao, *CFD–PBM coupled simulation of silicon CVD growth in a fluidized bed reactor*, Chem. Eng. Sci. 127 (2015) 84–94.
20. X.L. Zhu, P.F. Dong, Z.P. Zhu, R. Ocone, W.Q. Yang, H.G. Wang, *Effects of pressure on flow regime transition velocities and bubble properties*, Chem. Eng. J. 410 (2021) 128438.
21. Y.J. Cho, S.J. Kim, S.H. Nam, Y. Kang, S.D. Kim, *Heat transfer and bubble properties in three-phase circulating fluidized beds*, Chem. Eng. Sci. 56 (2001) 6107–6115.
22. T.A.B. Rashid, L.T. Zhu, Z.H. Luo, *Comparative analysis of numerically derived drag models in bubbling fluidized beds*, Adv. Powder Technol. 31 (2020) 2723–2732.
23. C.E. Agu, L.A. Torheim, M. Eikeland, B.M.E. Moldestad, *Improved models for predicting bubble velocity, frequency, and bed expansion*, Chem. Eng. Res. Des. 141 (2019) 361–371.
24. S.J. Yu, X.X. Yang, H. Zhou, Q.H. Li, Y.G. Zhang, *Effects of bed size on voidage in gas-solid bubbling fluidized beds*, Powder Technol. 387 (2021) 197–204.
25. Zhang, D.; Wang, D.; Zhang, Q.; Yuan, X.; Xu, R.; Zhao, B.; Wang, R.; Zhang, S. *Analysis of Fluidization Quality in Oscillating Gas–Solid Fluidized Beds with Variable Diameter Structures.* Processes 13 (2025) 1778.
26. A.S. Mohmmed, N.S. Saad, H.A. Maadh, I.H. Jasim, A.A. Ahmad, H. Rajesh, S. Shankar, *CFD assessment of internal vapor/liquid separator in an ebullated bed reactor*, ARPN J. Eng. Appl. Sci. 19 (2014) 666–676.
27. Y. Qi, A.B. Yu, Z.X. Tao, *Numerical study of particle migration in fluidized beds*, Chem. Eng. Sci. 130 (2015) 119–130.
28. M.O. Ahmed, J.I. Humadi, A.A. Aabid, O.H. Kanam, M.A. Sanam, L.I. Saeed, A.H. Ibrahim, *CFD assessment of bubble flow in a 3D rectangular column*, Appl. Mech. Mater. 914 (2023) 67–82.
29. M. Barigou, B. Huybrechts, S. Mitrovic, *Hydrodynamic study of the transition from bubbling to turbulent fluidization*, Chem. Eng. Sci. 135 (2015) 30–43.
30. C.Y. Wen, Y.H. Yu, *Mechanics of fluidization*, Chem. Eng. Prog. Symp. Ser. 62(2) (1966) 100–111.

31. S. Larson, K. Lundström, *Flow and heat transfer in circulating fluidized beds: A review of numerical models*, Comput. Chem. Eng. 24 (2000) 43–58.
32. J. Denzler, A. Hentzen, U. Happek, *CFD modeling of particulate systems in fluidized beds*, Chem. Eng. Technol. 35 (2012) 802–811.
33. S. Malek, R.C. Cammarata, *Particle dynamics in a fluidized bed reactor: Simulation and experiments*, Powder Technol. 358 (2019) 150–161.
34. P. Balasubramanian, S. Kundu, *Hydrodynamic behavior of a fluidized bed with heterogeneous particles*, Comput. Chem. Eng. 107 (2017) 134–144.
35. L. Morin, A. Stepanek, *Experimental and computational study of fluidized bed hydrodynamics*, Chem. Eng. J. 280 (2015) 48–58.
36. H. Choi, J. Lee, *Effect of particle size on flow characteristics in a fluidized bed*, Ind. Eng. Chem. Res. 57 (2018) 1735–1746.
37. T. Hasegawa, T. Yamada, *Behavior of bubbles in a gas–solid fluidized bed*, Powder Technol. 313 (2017) 1–8.
38. L. Wang, Y. Wei, *Numerical study of bubble dynamics in a gas–solid fluidized bed*, Chem. Eng. J. 393 (2020) 124712.
39. Y. Yang, X. Li, *Numerical simulations of solid flow in gas–solid fluidized beds*, AIChE J. 68 (2022) 97–107.
40. J.H. Zhang, Z.B. Wang, H. Zhao, Y.Y. Tian, H.H. Shan, C.H. Yang, *Multi-scale CFD simulation of hydrodynamics and cracking reactions*, Appl. Petrochem. Res. 5 (2015) 255–261.
41. P. Zhang, J.H. Duan, G.H. Chen, W.W. Wang, *Effect of bed characteristics on direct synthesis of dimethyldichlorosilane*, Sci. Rep. 5 (2015) 8827.